Mechanical behavior at elevated temperatures of an Al-Mn-Mg-Sc-Zr alloy manufactured by selective laser melting

D. Schliephake[a,b,*], D. Bayoumy[a], S. Seils[b,c], C. Schulz[b], A. Kauffmann[b], X. Wu[a], A.J. Huang[a]

[a] Monash Centre for Additive Manufacturing (MCAM), Monash University, 15-17 Normanby Rd, Notting Hill, VIC 3168, Australia

[b] Institute for Applied Materials (IAM-WK), Karlsruhe Institute of Technology (KIT), Engelbert-Arnold-Str. 4, D-76131 Karlsruhe, Germany

[c] Karlsruhe Nano Micro Facility (KNMF), Karlsruhe Institute of Technology (KIT), Hermann-von-Helmholtz-Platz 1, D-76344 Eggenstein-Leopoldshafen, Germany

* Corresponding author: daniel.schliephake@kit.edu

Abstract

A high temperature compression and compression creep study was undertaken performed on Al-Mn-Mg-Sc-Zr alloy produced by selective laser melting (SLM). High temperature compression tests in the temperature range from 150 to 300 °C were conducted for the as-fabricated (AF) and aged (HT) SLM specimens. The 0.2% proof stress ($\sigma_{0.2}$) showed comparable values at different loading directions, which reveal an isotropic mechanical behavior. $\sigma_{0.2}$ of the HT samples exceeded that of the AF at temperatures up to 200 °C. At 250 °C, $\sigma_{0.2}$ of AF surpasses that of HT, due to the interaction of solid solution strengthening above 0.5 of the homologous temperature and the formation of new precipitates in this temperature range. For AF and HT $\sigma_{0.2}$ becomes similar again at 300 °C. Creep tests were conducted at 250 °C in a stress range of 100 to 150 MPa. The Norton stress exponent was determined to (5.1 ± 0.2) indicating that creep is dislocation climb controlled. An activation energy for creep of (198 ± 11) kJ/mol was found. It is suggested that solid solution strengthening in conjunction with a dispersed $L1_2$ Al_3Sc precipitates improved the creep resistance compared to conventionally cast-manufactured Al-Sc-Zr alloys.

Keywords: Aluminum alloy; Selective Laser Melting; Precipitation Hardening; Mechanical Properties; Elevated Temperatures

Introduction

Selective laser melting (SLM) exhibits enormous benefits for the development of precipitation-strengthened Al alloys for structural high-temperature applications [1-3]. Despite the conventional aspects associated with SLM processes, namely the higher freedom of design, minimized machining efforts and rapid prototyping [4], SLM allows for the formation of supersaturated solid solutions and very fine microstructures to improve the mechanical properties which are thermally stable as well [5-7]. However, this does not apply to any Al alloy due to the nature of the process that can be simplified as multipass welding. On the one hand, Al-Mg-Si based 6000 series alloys or Al-Zn-Mg based 7000 series alloys, for example, suffer from hot cracking due to the rapid solidification in SLM and their large freezing zones [8,9]. Al-Si alloys, on the other hand, are well suited for SLM [10-12], but they possess relatively low strength and ductility compared to precipitation-strengthened Al alloys. Recently, high-strength Al-Si-Ni-Fe [13] and Al-3Ce-7Cu [14] alloys manufactured by selective laser melting have been introduced. However, both alloys are not suited for precipitation strengthening and especially the hardness of the Al-3Ce-7Cu alloy significantly decreases after heat treatments at 250 °C and above [14]. Therefore, the research on precipitation-strengthened Al alloys suited for SLM

has led to the development of novel high-strength Al alloys strengthened by $L1_2$ precipitates. The most prominent example is the commercially available Scalmalloy®, which is an Al-Mg-Sc-Zr based alloy [1,15,16]. Sc is known to be one of the most effective alloying elements in Al due to the formation of Al_3Sc ($L1_2$) precipitates [17]. The low diffusion coefficient of Sc, as well as the high coherence and low lattice mismatch of Al_3Sc to the matrix provide an exceptionally good thermal stability of the precipitates [17,18]. Furthermore, the grain size is significantly reduced in hypereutectic Al-Sc alloys due to the primary solidification von Al_3Sc particles that act as nucleation sides [19]. Additional alloying with Zr leads to the formation of $Al_3(Sc,Zr)$ precipitates, where Zr substitute Sc and decreases the lattice mismatch even further and increases the thermal stability of the precipitates [17,20]. Besides Scalmalloy®, research has been conducted on alloys with higher Mg and lower Sc and Zr contents encouraged by the high costs of Sc [21-24]. Other $L1_2$ precipitate-forming Al-alloys are Al-Mn-Mg-Sc-Zr [2,25,26], where Mn substitutes a large portion of Mg to improve solid solution strengthening and the Sc-free Addalloy®, which is based on Al-Mg-Zr [3,7,27]. The later forms Al_3Zr with a metastable $L1_2$ crystal structure by the high cooling rates during SLM instead of stable Al_3Sc precipitates.

Even though those alloys were developed for high-temperature applications, little is known about the mechanical properties at elevated temperatures. The strengthening effect and creep behavior of binary Al-Sc cast alloys are well investigated [17,28,29], but SLM-processed alloys exhibit a different microstructure due to the processing. It is known that SLM can lead to a crystallographic texture formation along the build direction in Al-alloys [4,11,30]. Additionally, the microstructure of precipitation strengthened alloys consist of a bimodal grain structure with fine and equiaxed grains at the bottom of the melt pool and elongated grains in a fan-like morphology almost along the solidification direction [25]. Therefore, the mechanical response at higher temperatures might differ from the behavior of cast binary Al-Sc alloys. Bi et al. [21,22] have investigated the mechanical behavior of a Mg-rich Al-Mg-Si-Sc-Zr alloy at temperatures up to 400 °C in the as-fabricated condition. However, the authors have not investigated the creep behavior of the alloy. Recently, Griffiths et al. [7] investigated the creep resistance of SLM processed Al-Mg-Zr forming Al_3Zr precipitates with a metastable $L1_2$ crystal structure in as-fabricated and peak-aged (400 °C/8 h) condition. They found continuous precipitates with spheroidal shape and a diameter of approx. 2 nm and discontinuous precipitates of 5 nm width and hundreds of nanometers in length. The authors identified the creep mechanism based on the stress exponent between 2 and 3 to be dominated by grain boundary sliding or dislocation motion. The possible influence of the different grain morphologies was not addressed.

Hence, this work aims to investigate the mechanical properties of an Al-4.58Mn-1.24Mg-0.91Sc-0.42Zr alloy at elevated temperatures. Bayoumy et al. [25] have recently shown, that this alloy can be manufactured with a density above 99.8% under various processing conditions by SLM (i.e., laser power and scan speed). Furthermore, if this alloy is manufactured by SLM, it exceeds the room-temperature strength of other Sc-containing Al alloys and is therefore a promising candidate for high-temperature applications.

Experimental

In this work, we investigate the mechanical behavior at high-temperatures of an $L1_2$ strengthened Sc-containing alloy manufactured by SLM. For this, an EOS M290 machine was used to manufacture 20 x 20 x 20 mm³ blocks of the Al-Mn-Mg-Sc-Zr alloy. Details about the powder characterization and process-optimization can be found elsewhere [25]. Samples were built at a laser power of 350 W and a scan speed of 1600 mm/s to achieve a density above 99.8 %. The hatch distance was kept at 0.1 mm and the layer thickness was 30 µm. All samples were manufactured under an Ar atmosphere and a scan track rotation of 67° alternating between consecutive layers. ICP-OES was used to analyze the chemical composition of the as-fabricated alloy, which is given in Tab 1. In this work, the Al-Mn-Mg-Sc-

Zr alloy was investigated in two different conditions, namely as-fabricated AF and peak-aged HT300 at 300°C for 6 h in air followed by water-quenching. AF was tested along the build direction (BD) and HT300 along and perpendicular to build direction, denoted by HT300L and HT300T, respectively. A Qness Q10+ micro-hardness tester was used to measure the micro-hardness before and after aging for various times up to 600 min on polished samples with a 1 µm surface finish.

Samples of 5 x 3 x 3 mm³ in dimensions for mechanical testing were prepared by electrical discharge machining. Compression tests were performed using a UPM-Zwick 1478 universal testing device with an induction coil to heat the samples up to testing temperatures ranging from 150 to 300 °C. All tests were started after sufficient holding time of 15 min at test temperature to ensure the temperature being evenly distributed. The initial strain rate was set to $1 \cdot 10^{-3}\ s^{-1}$. The compression creep tests were performed at constant load corresponding to initial engineering stresses of 100, 125 and 150 MPa at 250 °C. Additional creep tests were performed at 225 and 275 °C at an initial stress of 125 MPa to determine the activation energy for creep. All mechanical tests were done in air. Since the compression creep tests were performed at constant load, the true stress decreases during deformation due to increasing sample cross section (geometrical hardening). Hence, creep rates in the steady-state decrease continuously with increasing strain. Therefore, the true creep rate for a fictive constant true stress (corresponding to the engineering stress) is calculated based on the procedure described in what follows.

The true steady-state creep rate $\dot{\bar{\varepsilon}}_t$ as a function of constant true stress $\bar{\sigma}_t$ is expressed by the Norton creep law:

$$\dot{\bar{\varepsilon}}_t = A \cdot \bar{\sigma}_t^n \tag{1}$$

A and n are a constant and the stress exponent, respectively. The creep rate $\dot{\tilde{\varepsilon}}_t(\tilde{\varepsilon}_t)$ obtained in a test with changing true stress $\tilde{\sigma}_t(\tilde{\varepsilon}_t)$ might be approximated by the Norton law:

$$\dot{\tilde{\varepsilon}}_t(\tilde{\varepsilon}_t) \approx A \cdot \tilde{\sigma}_t^n(\tilde{\varepsilon}_t) \tag{2}$$

when assuming that A and n are constant in the entire strain range and for small changes in true stress. Equs. (1) and (2) can be combined to

$$\dot{\bar{\varepsilon}}_t = \frac{\bar{\sigma}_t^n}{\tilde{\sigma}_t^n(\tilde{\varepsilon}_t)} \cdot \dot{\tilde{\varepsilon}}_t(\tilde{\varepsilon}_t) \tag{3}$$

By assuming a prismatic sample shape and volume preservation the true quantities $\dot{\tilde{\varepsilon}}_t$ and $\tilde{\sigma}_t$ can be replaced by the engineering quantities obtained throughout the test:

$$\tilde{\sigma}_t = \tilde{\sigma}_e(1 + \tilde{\varepsilon}_e) \tag{4}$$

$$\tilde{\varepsilon}_t = \ln(1 + \tilde{\varepsilon}_e) \tag{5}$$

$$\dot{\tilde{\varepsilon}}_t = \frac{\dot{\tilde{\varepsilon}}_e}{1 + \tilde{\varepsilon}_e} \tag{6}$$

Eq. (3) becomes:

$$\dot{\bar{\varepsilon}}_t = \frac{\bar{\sigma}_t^n}{\tilde{\sigma}_e^n} \cdot \frac{\dot{\tilde{\varepsilon}}_e}{(1 + \tilde{\varepsilon}_e)^{n+1}} \tag{7}$$

For a test at constant initial load corresponding to $\bar{\sigma}_t = \tilde{\sigma}_e = \sigma_0$, a correction of the form

$$\dot{\bar{\varepsilon}}_t = \frac{\dot{\tilde{\varepsilon}}_e}{(1 + \tilde{\varepsilon}_e)^{n+1}} \tag{8}$$

might be performed. The stress exponent n was estimated 4.8 at 10 % engineering strain. In the transient region, the approximation of $\dot{\tilde{\varepsilon}}_t(\tilde{\varepsilon}_t)$ in Eq. (2) with the Norton law will fail to describe the situation properly since no steady state is achieve. Anyhow, the strains remain below 5 % of true strain. This corresponds to a lower true stress of minimum 142 MPa in the

case of 150 MPa engineering stress. The deviation of the approximated creep rate with respect to a constant true stress creep experiment remains below 5 %. In the steady state, the difference in engineering stress $\tilde{\sigma}_e$ and true stress $\tilde{\sigma}_t$ make up to 20 MPa. The correction is then up to 14 % of the experimentally observed creep rate $\dot{\tilde{\varepsilon}}_e$ or $\dot{\tilde{\varepsilon}}_t$.

Table 1: Chemical composition in wt.% analysed by ICP-OES of AF

	Al	Mn	Mg	Sc	Zr	Fe	Si
wt.%	rest	4.58	1.24	0.91	0.42	0.07	0.04

Microstructural analysis was performed on samples prepared by grinding with progressively finer SiC grits before final polishing with a colloidal silica solution. A JEOL 7001F FEG scanning electron microscope was used in backscattered electron mode (BSE) to examine the microstructure in the conditions prior to mechanical tests. After creep testing, the microstructure was analyzed using a Zeiss LEO 1530 FEG scanning electron microscope. The grain size was determined utilizing the interception method on at least ten micrographs. The volume fraction of precipitates was determined on binarized BSE micrographs.

Results

The microstructure of AF is shown in the BSE micrographs in Fig. 1 (a). The melt-pool morphology can be clearly identified by two different grain morphologies. While the bottom of the melt-pool consists of equiaxed grains with a grain size of (0.49 ± 0.05) µm, grains in the center to upper region are elongated in a fan-shaped morphology along the solidification direction in the melt pool by up to 50 µm at a maximum aspect ratio of approximately 10. A high number of bright precipitates (blue arrows) can be found in the equiaxed region compared to the region of elongated grains. In our previous work on the same alloy under the same processing conditions [25], those bright precipitates are described in detail. They were found to be a quasicrystalline and rich in Mn and Fe. Investigations by Jia et al. [26] on a similar alloy further revealed a stoichiometry of Al_6Mn for this phase.

Besides those bright precipitates, primary solidified Al_3Sc can be found with bright contrast (marked with red arrows in Fig. 1 (b)). Both types of precipitates make up for a total of (6.9 ± 0.6) vol.% in the fine-grained region, while the coarse, elongated grains contain only (2.2 ± 0.3) vol.% of precipitates. Fig. 1 (c) and (d) display the microstructure of HT300. The grain size of the equiaxed grains slightly increases during peak aging to (0.58 ± 0.06) µm. The total volume fraction of both types of precipitates increases to (7.2 ± 0.7) vol.% and (2.4 ± 0.4) vol.% for the regions of fine and elongated grains, respectively. Therefore, the total volume fraction of precipitates is increasing during the aging heat treatment at 300 °C as well. As a consequence, the Al solid solution matrix is less enriched with Mn and Sc. The columnar grains have globular cross section of (1.3 ± 0.2) µm in diameter perpendicular to the BD in the HT300T condition, as can be seen in Fig. 1 (d).

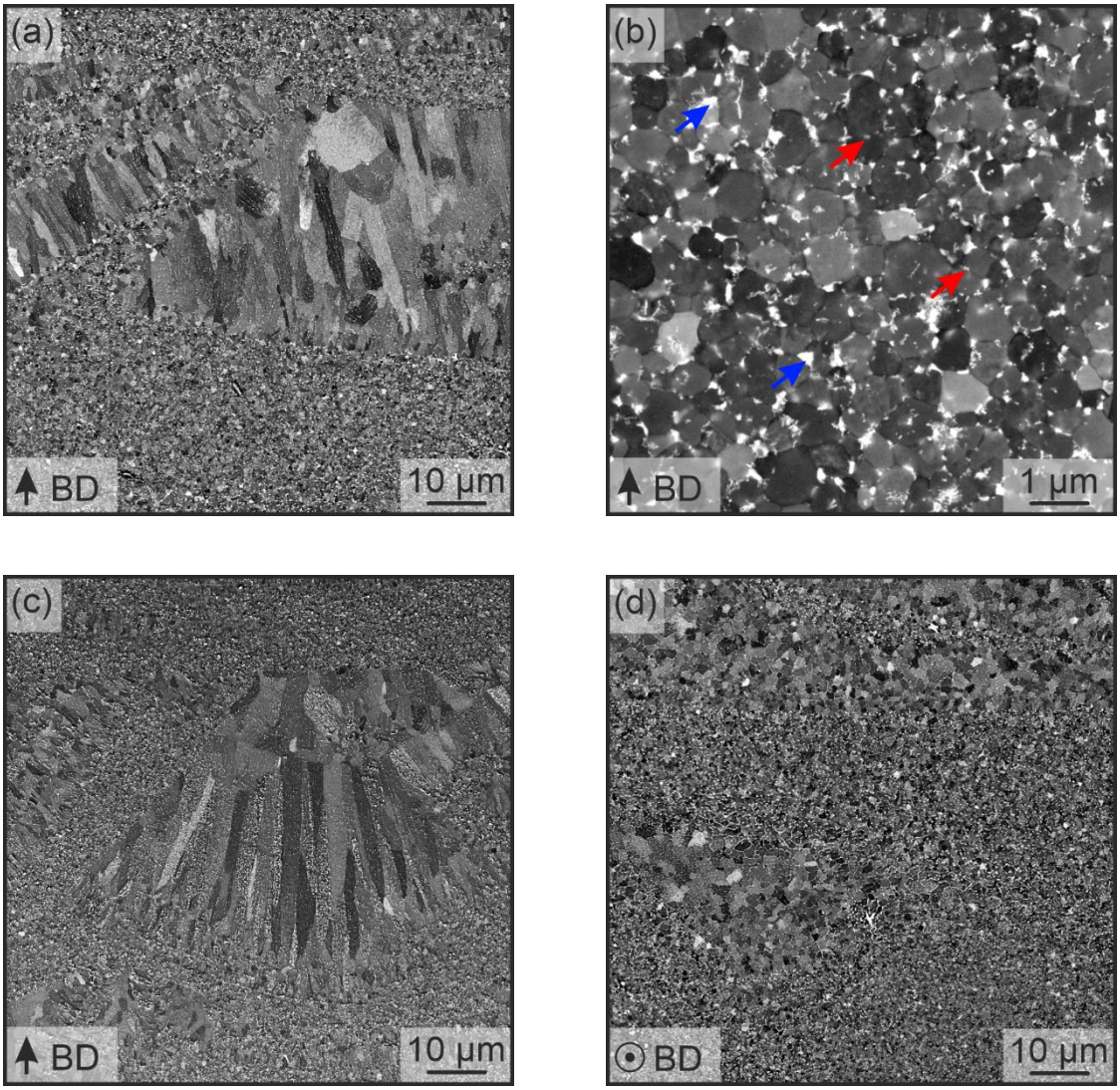

Figure 1: BSE micrographs: (a) overview of AF with BD vertical in the image, (b) details of the fine-grained region in AF showing primary Al_6Mn (bright particles marked by blue arrows) and primary solidified Al_3Sc (bright grey particles marked with red arrow), and HT300with (c) BD vertical and (d) BD out of plane of projection.

Fig. 2 (a-e) displays the compressive stress-strain curves of AF, HT300T and HT300L depending on the temperature. Only one representative curve of in total three tests performed for each condition and test temperature is shown for the sake of clarity. In Fig. 2 (f), the mean compressive 0.2 % offset yield stress ($\sigma_{0.2}$) depending on the test temperature is depicted. As expected, AF possesses a lower $\sigma_{0.2}$ at room temperature compared to HT300. However, the difference between $\sigma_{0.2}$ of the AF and HT300 becomes smaller with increasing temperature up to 200 °C. At 250 °C, $\sigma_{0.2}$ of AF is significantly higher than for both test directions of HT300, but becomes similar at 300 °C. It is worth mentioning, that no difference in yield strength was observed for the HT300L and HT300T samples, suggesting that the mechanical behavior remains independent from the test direction.

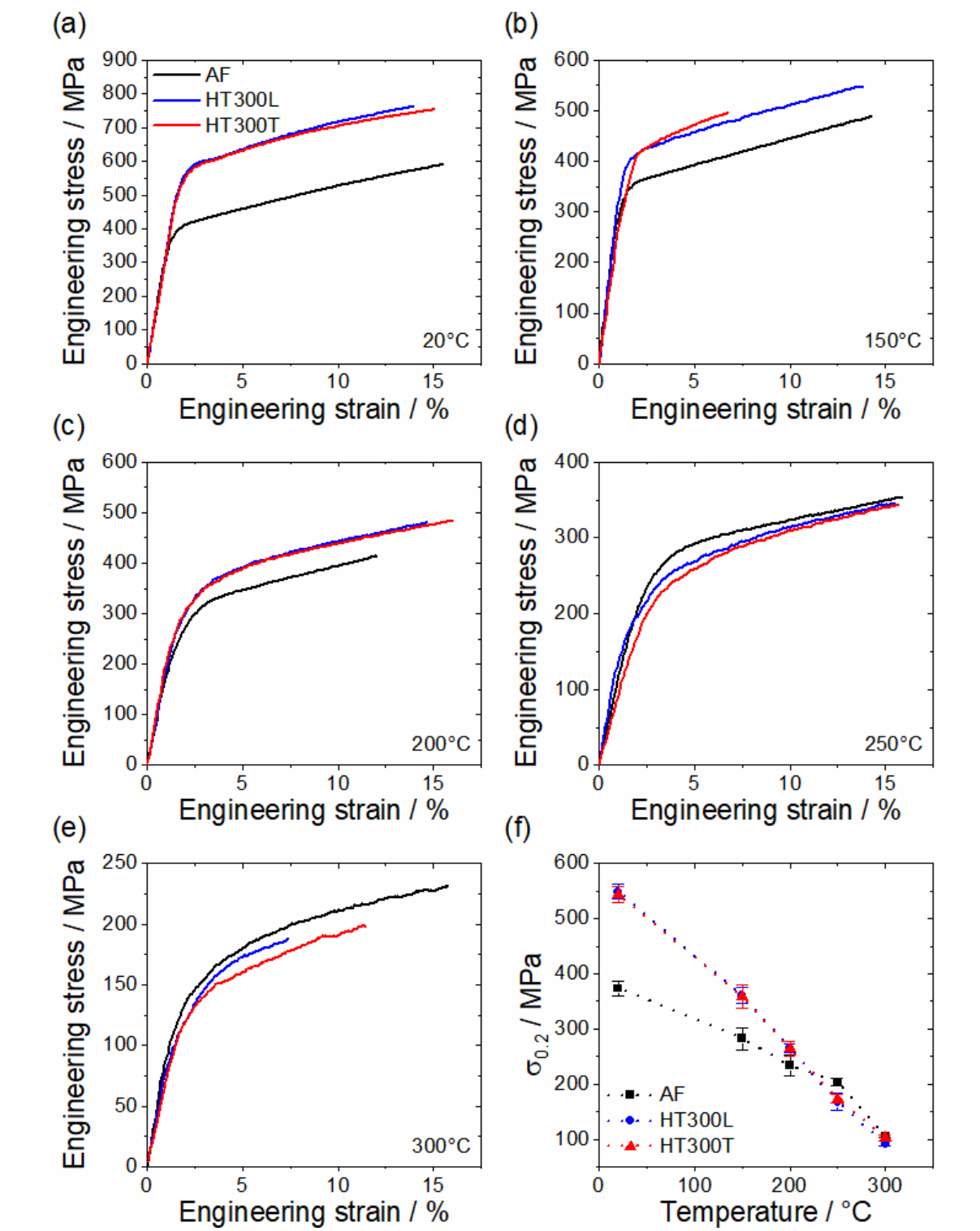

Figure 2: (a-e) Compressive strain-stress curves of AF, HT300L and HT300T at temperatures ranging from 20 °C to 300 °C and (f) temperature-dependent compressive 0.2% offset yield strength $\sigma_{0.2}$.

To evaluate a possible influence of the exposure time at test temperature before the compression tests, the hardness response after aging of AF at 200, 250 and 300 °C was investigated and the results are shown in Fig. 3. It can be seen, that it takes at least 120 min before the hardness of the alloy exposed to 200 °C starts to increase significantly, while it takes less than 15 min at 250 and 300 °C.

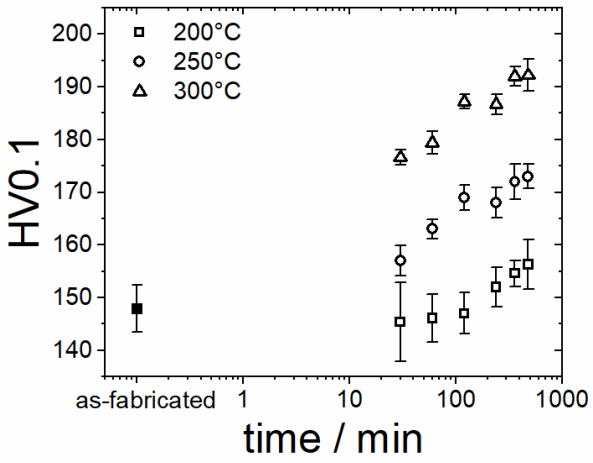

Figure 3: Age hardening response of AF for aging at 200, 250 and 300 °C.

Fig. 4 (a) depicts the true compressive creep rates as a function of true strain at 250 °C of the HT300L alloy for stresses ranging from 100 to 150 MPa. By increasing stress, the creep rates become larger. The steady-state creep rate is attained after 6 - 10 % true strain for all tested samples (also for the HT300L and HT300T conditions, not shown here). Fig. 4 (b) summarizes the true creep rates in dependence of the true compressive stress in the double-logarithmic Norton plot. The creep tests are in accordance with the compression tests at 250 °C. While both peak-aged conditions possess similar creep rates, AF shows creep rates by half an order of magnitude lower over the tested stress range. The apparent stress exponent $n_t = 5.1 \pm 0.2$ for the constant true stress condition was determined from the slope in Fig. 4 (b) for each test condition. It reveals similar dominant creep mechanisms independent from the heat treatment applied prior to the creep tests and the orientation of the compression direction to the build direction.

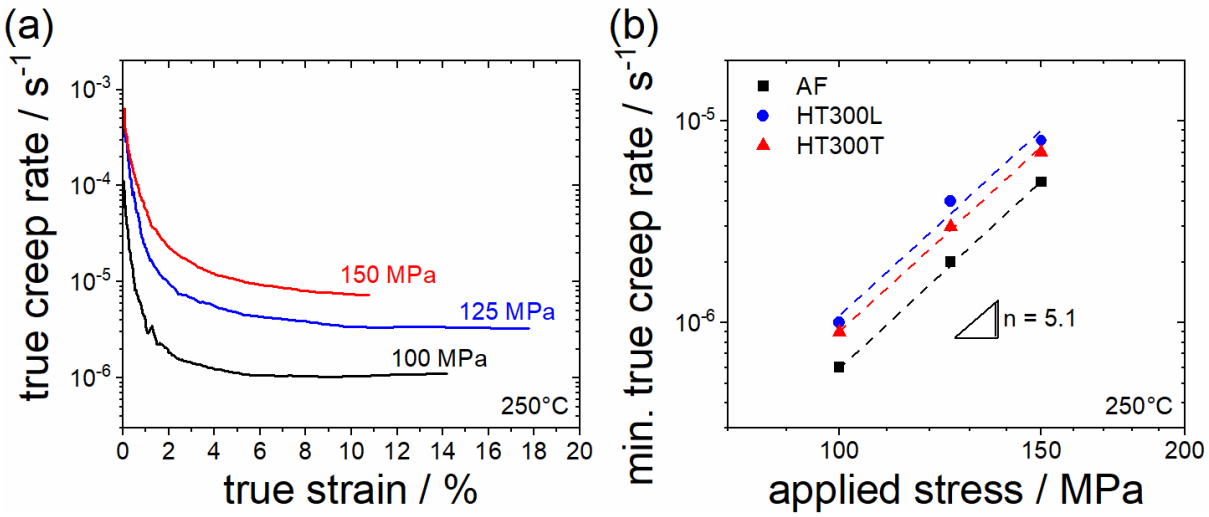

Figure 4: Compressive creep behaviour at 250 °C: (a) compressive creep curves at 100, 125 and 150 MPa of AF and (b) the corresponding Norton Plot for AF and HT300 along (HT300L) and perpendicular (HT300T) to the build direction.

Fig. 5 (a-d) depicts the microstructure before and after creep deformation of the coarse-grained regions in HT300L and HT300T. All regions, including the coarse-grained region significantly participate to creep deformation. New grains have been formed during the deformation process, which can be identified by the dark contrast and the absence of Al_6Mn precipitates in the grain interior. The lower volume fraction of precipitates within the coarse grains compared

to the fine-grained region leads to a lower creep resistance and therefore, a significant contribution to creep deformation. The fine grains change their shape and are clinched perpendicular to the applied stress, as shown in Fig. 5 (e). The high amount of Al_6Mn particles impede grain rotation by boundary sliding and promote the grain shape change. The apparent activation energy for creep $\dot{Q}_C$ based on the Arrhenius term for $\dot{\bar{\varepsilon}}_t$:

$$\dot{\bar{\varepsilon}}_t \sim e^{-\frac{\dot{Q}_C}{RT}} \tag{6}$$

of AF is (198 ± 11) kJ/mol in a temperature range of 225 to 275 °C and a stress of 125 MPa.

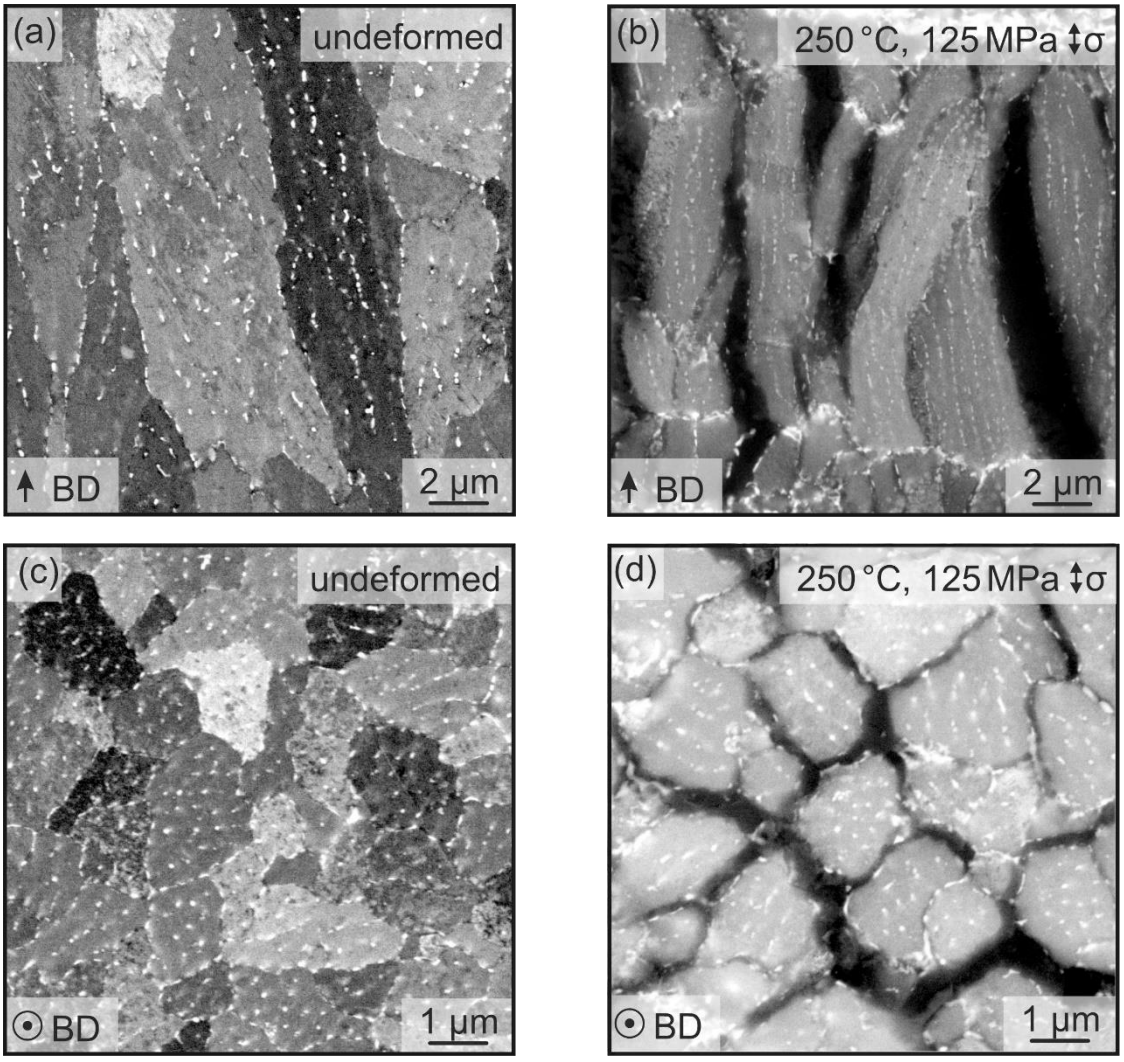

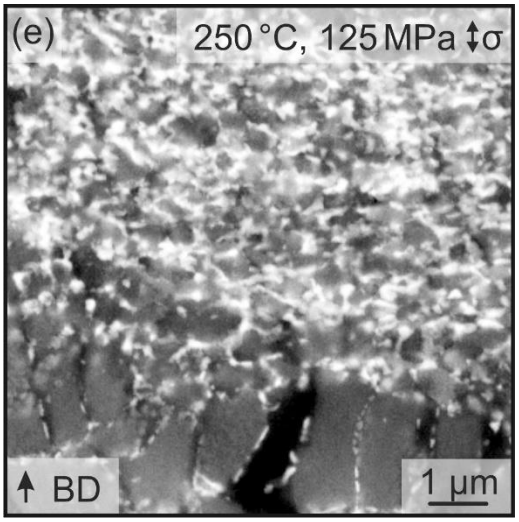

Figure 5: BSE micrographs of HT300L and HT300T: (a,c) before creep testing, (b,d,e) after 15 % creep strain (in vertical direction) at 250 °C and 125 MPa. (a,b,e) with BD being vertical and (c,d) with BD being out of the plane of projection.

Discussion

The higher strength of AF at 250 °C is unexpected, but the almost similar yield strength of both conditions, AF and HT300, at 300 °C suggests that this might be related to the precipitation in the early stages of testing. As mentioned earlier, the compression tests started approximately 15 min after reaching the respective temperature for testing to ensure thermal equilibrium. Jia et al. [26] found Al_3Sc forming mainly in the early stages of the peak-aging heat treatment at 300 °C. Following those results, the Al_3Sc phase starts forming and coarsening within the first few minutes in a similar Al-Mn-Mg-Sc-Zr alloy at 300 °C. We found that in this work the volume fraction of the precipitates slightly increases during peak-aging heat treatment in the fine-grained region as well as in the coarse-grained region (see above), reducing the number of solute atoms in the Al-matrix. This leads to a larger strengthening effect by precipitates on the one hand, but on the other hand, it decreases the amount of solid solution strengthening mainly by Sc and Mn atoms in the Al matrix. Furthermore, the Al_6Mn precipitates are majorly located at the grain boundaries and therefore do not contribute directly to the strengthening of the alloy, besides the fact that they prevent grain growth during the aging treatment. The hardness response during exposure time at test temperatures revealed that AF already starts to increase hardness and therefore its $\sigma_{0.2}$ just due to the exposure of 250 and 300 °C for 15 min before the compression test actually starts. However, AF is not reaching the maximum hardness value. Hence, the solid solution in the AF condition will still have more Mn and Sc solved compared to the conditions in HT300L and HT300T. Furthermore, at testing temperatures T of 200 °C and above the homologous temperature $T_{\mathrm{hom}} = T/T_m$ (with T_m being the solidus temperature) surpasses 0.5, which means that diffusion-controlled dislocation climb to overcome obstacles like Al_3Sc precipitates becomes significant as will be shown during the discussion of the creep experiments later in this work. With all this information we assume the yield strength of AF to be influenced by contrary effects: (i) Exposure at 250 °C and 300 °C, while waiting for thermal equilibrium, leads to the formation of additional Al_3Sc precipitates and therefore an increase in strength. (ii) The increase of the volume fraction of precipitates leads to a depletion in Sc and Mn in the matrix and therefore a decrease in the solid solution strengthening. (iii) Dislocations climb at higher temperatures to overcome obstacles is activated. Moreover, Griffiths et al. [7] have observed a similar behavior for the Al-Mg-Zr alloy, where they found a higher yield strength of AF above 177 °C compared to the peak-aged condition (400 °C/8 h). In addition, they found a similar creep behavior of both conditions after an additional exposure of 120 h at 260 °C and concluded that aging occurred during the

additional heat treatment [7]. However, their creep data is well fitted by a stress exponent n = 2 or 3, which is indicative of grain boundary gliding or dislocation gliding [7]. In the present alloy the apparent stress exponent indicates that dislocation climb controls steady state creep in good agreement with data published by Seidman et al. [29]. A creep exponent of 4.4 was found for cast Al-0.3 wt.% Sc tested at temperatures ranging from 225 to 300 °C [29]. Therefore, grain boundary sliding, as previously reported in additive manufactured and precipitation strengthened ultrafine-grained Al alloys can be excluded [7], since the stress exponent for grain boundary sliding is generally associated to values close to $n = 2$ [31]. In addition, the high amount of grain boundary precipitates (Al_6Mn and Al_3Sc) is expected to prevent grain boundary sliding or strain accommodation by grain rotation.

The apparent activation energy for creep is higher than previously reported $\dot{Q}_C$ of 132 kJ/mol for dislocation climb controlled creep in Al [32] and 138 kJ/mol for Al-0.3 wt.% Sc [29]. For the present alloy the influence of Mg and Mn has to be considered. The activation energy for diffusion of Mg in Al is 120 kJ/mol [33]. This is lower than the above mentioned low $\dot{Q}_C$ for creep of Al, Al-Sc and AF. Hence, dissolved Mg does not contribute to a substantial decrease in $\dot{Q}_C$. The activation energy of diffusion of Mn in Al of 211 kJ/mol [34] is close to the determined activation energy of (198 ± 11) kJ/mol in this work. Therefore, Mn seems to contribute to the rather high $\dot{Q}_C$ of AF, if it is dissolved in the solid solution. Jia et al. [26] suggest, that the formation of Al_6Mn is not effectively activated by annealing at 300 °C for 5 hours, but starts significantly at 350 °C. In this work we have shown, that the volume fraction of precipitates is only slightly increasing without distinguishing between Al_3Sc and Al_6Mn at 300 °C for 6 h. For this reason, the decomposition of the Mn-rich solid solution is believed to be negligible at 250 °C, where the creep tests have been performed, even though the duration of the creep tests was up to 80 h. Therefore, Mn indeed remains mainly in solid. A similar apparent activation energy of creep in the investigated alloy compared to the activation energy of Mn diffusion in Al is supporting the identification of dislocation climb controlled creep based on the Norton exponent. As proposed by Cottrell [35], the distortion field of solute atoms might pin dislocations. To further move the dislocation without increasing the applied stress, the Mn solute atom has to diffuse away from the dislocation.

Compared to other $L1_2$ precipitation strengthened Al alloys manufactured by SLM, the Al-Mn-Mg-Sc-Zr alloy investigated in the present work shows a superior creep behavior in the AF as well as in the HT condition compared to other $L1_2$ strengthened Al-alloys, such as cast-manufactured Al-Sc and Al-Sc-Zr [20,29] and additively manufactured Al-Mg-Zr [7]. This can be explained (i) by the influence of the solute Mn in the matrix and (ii) by a higher number density of Al_3Sc precipitates compared to other commonly investigated Al alloys. For example, the published creep rates for Al-Mg-Zr at 260 °C are at least 5 orders of magnitude higher [7]. The creep tests performed at 275 °C and 125 MPa to determine the apparent activation energy for creep display a significant lower true creep rate compared to the published creep rates of Al-Mg-Zr at 260°C. Hence, the difference of 10 K does not rationalize such a significant difference. Although the Al-Mg-Zr alloy possess 2.9 wt.% Mg, the solid solution strengthening to increase the creep resistance is less effective than for the Mn addition of the alloy in this work, as can be seen by the lower activation energy for Mg diffusion in Al. It has been reported recently, that the strength contribution of solid solution in the peak-aged condition for the Al-Mn-Mg-Sc-Zr alloy is up to approx. 134 MPa at room temperature [2]. This even exceeds the solid solution strengthening effect in the widely applied alloy 7075, where high amounts of up to 10 wt.% in total of dissolved Zn, Mg and Cu can increase yield strength by approx. 82 MPa [36]. Despite the $L1_2$ precipitates, solid solution strengthening has a huge contribution in increasing the creep resistance at 250 °C, as we have shown by the lower creep rates of the AF condition compared to HT300. Furthermore, the creep rates of the investigated Al-Mn-Mg-Sc-Zr alloy are lower compared to conventionally cast-manufactured Al-Sc alloys [29]. These

alloys typically contain up to 0.3 wt.% Sc compared to 0.91 wt.% Sc in the present alloy. Therefore, a lower number density of Al_3Sc particles can be expected, resulting in a lower creep resistance. Even though the creep resistance of the peak-aged conditions is half an order of magnitude lower than for AF, the yield strength is significantly higher below 250 °C. Therefore, the heat treatment condition has to be adjusted to the actual application of the parts.

Summary and Conclusions

In this work, we reported on the high temperature properties in compression of an additively manufactured Al-Mn-Mg-Sc-Zr alloy in different conditions. First of all, two different directions, namely vertical and transversal to the build direction have been examined in terms of microstructure, compression and compression creep properties. Both build orientations possess a bimodal microstructure, even though in the transversal direction both grain fractions are equiaxed, while the coarser grains are elongated along the build direction in case of the vertical orientation. However, this does not affect the mechanical properties for the peak-aged condition, since the compression strength and creep resistance are independent of the build direction when macroscopic test samples are considered. The aged conditions both possess a higher offset yield strength $\sigma_{0.2}$ compared to AF up to 200 °C. However, the $\sigma_{0.2}$ of AF exceeds those of the aged ones at 250 °C before becoming similar for all conditions at 300 °C. The higher strength at 250 °C is a result of the higher content of Sc and Mn in solid solution for AF compared to the solid solution of the aged condition. Dislocation climb controlled creep is majorly responsible for creep deformation in the present alloy as indicated by the determined apparent stress exponent n_t of 5.1 ± 0.2 and the apparent activation energy of (198 ± 11) kJ/mol. Despite the high amount of Sc and therefore Al_3Sc precipitates compared to conventional casted Al-Sc in literature, the high Mn content in the investigated Al-Mn-Mg-Sc-Zr alloy is also assumed to be responsible for its higher creep resistance compared to other Al alloys.

Acknowledgements

The authors gratefully acknowledge financial support from the Australian Research Council grant number IH130100008 “Industrial Transformation Research Hub for Transforming Australia's Manufacturing Industry through High Value Additive Manufacturing”. The use of facilities within Monash Centre for Electron Microscopy (MCEM) is also acknowledged.

Research data for this article

The raw/processed data required to reproduce these findings cannot be shared at this time as the data also forms part of an ongoing study.

References

[1] A.B. Spierings, K. Dawson, M. Voegtlin, F. Palm, P.J. Uggowitzer, Microstructure and mechanical properties of as-processed scandium modified aluminium using selective laser melting, CIRP Ann. Manuf. Technol. 65 (2016) 213–216. https://doi.org/10.1016/j.cirp.2016.04.057

[2] Q. Jia, P. Rometsch, P. Kürnsteiner, Q. Chao, A. Huang, M. Weyland, L. Bourgeois, X. Wu, Selective laser melting of a high strength AlMnSc alloy: alloy design and strengthening mechanisms, Acta Mater. 171 (2019) 43–445. https://doi.org/10.1016/j.actamat.2019.04.014

[3] J.R. Corteau, S. Griffiths, M.D. Rossell, C. Leinenbach, C. Kenel, V. Jansen, D.N. Seidman, D.C. Dunand, N.Q. Vo, Microstructure and mechanical properties of Al-Mg-Zr alloys processed by selective laser melting, Acta Mater. 153 (2018) 35–44. https://doi.org/10.1016/j.actamat.2018.04.053

[4] L. Bian, N. Shamsaei, J.M. Usher, Laser-Based Additive Manufacturing of Metal Parts: Modeling, Optimization, and Control of Mechanical Properties, CRC Press, London, New York, (2017).

[5] Y. Shi, P. Rometsch, K. Yang, F. Palm, X. Wu, Characterization of a novel Sc and Zr modified Al-Mg alloy fabricated by selective laser melting, Mater. Lett. 196 (2017) 34–350. https://doi.org/10.1016/j.matlet.2017.03.089

[6] X.P. Li, X.J. Wang, M. Suanders, A. Suvorova, L.C. Zhang, Y.J. Liu, M.H. Fang, Z.H. Huang, T.B. Sercombe, A selective laser melting and solution heat treatment refined Al-12Si alloy with a controllable ultrafine eutectic microstructure and 25% tensile ductility, Acta Mater. 95 (2015) 74–82. https://doi.org/10.1016/j.actamat.2015.05.017

[7] S. Griffiths, J.R Corteau, M.D. Rossell, R. Erni, A. De Luca, N.Q. Vo, D.C. Dunand, C. Leinenbach, Coarsening- and creep resistance of precipitation-strengthened Al-Mg-Zr alloys processed by selective laser melting, Acta Mater. 188 (2020) 192–202. https://doi.org/10.1016/j.actamat.2020.02.008

[8] N. Kaufmann, M. Imran, T.M. Wischeropp, C. Emmelmann, S. Siddique, F. Walther, Influence of process parameters on the quality of aluminium alloy EN AW 7075 using selective laser melting (SLM), Physics Procedia 83 (2016) 918–926. https://doi.org/10.1016/j.phpro.2016.08.096

[9] H. Zhang, H. Zhu, T. Qi, Z. Hu, X. Zeng, Selective laser melting of high strength Al-Cu-Mg alloys: Processing, microstructure and mechanical properties, Mater. Sci. Eng. A 656 (2016) 47–54. https://doi.org/10.1016/j.msea.2015.12.101

[10] N.T. Aboulkhair, I. Maskery, C. Tuck, I. Ashcroft, N.M. Everitt, On the formation of AlSi10Mg single tracks and layers in selective laser melting: Microstructure and nanomechanical properties, J. of Mater. Process. Technol. 230 (2016) 88–98. https://doi.org/10.1016/j.jmatprotec.2015.11.016

[11] U. Tradowsky, J. White, R.M. Ward, N. Read, W. Reimers, M.M. Attallah, Selective laser melting of AlSi10Mg: Influence of post-processing on the microstructural and tensile properties development, Mater. Des. 105 (2016) 212–222. https://doi.org/10.1016/j.matdes.2016.05.066

[12] N. Read, W. Wang, K. Essa, M.M. Attallah, Selective laser melting of AlSi10Mg alloy: Process optimisation and mechanical properties development, Mater. Des. 65 (2015) 417–424. https://doi.org/10.1016/j.matdes.2014.09.044

[13] D.R. Manca, A.Yu. Churyumov, A.V. Pozdniakov, D.K. Ryabov, V.A. Korolev, D.K. Daubarayte, Novel heat-resistant Al-Si-Ni-Fe alloy manufactured by selective laser melting, Mater. Lett. 236 (2019) 676–679. https://doi.org/10.1016/j.matlet.2018.11.033

[14] D.R. Manca, A.Yu. Churyumov, A.V. Pozdniakov, A.S. Prosviryakov, D.K. Ryabov, A.Yu. Krokhin, V.A. Korolev, D.K. Daubarayte, Microstructure and Properties of Novel Heat Resistant Al–Ce–Cu Alloy for Additive Manufacturing, Met. Mater. Int. 25 (2019) 633–640. https://doi.org/10.1007/s12540-018-00211-0

[15] A.B. Spierings, K. Dawson, T. Heeling, P.J. Uggowitzer, R. Schäublin, F. Palm, K. Wegener, Microstructural features of Sc- and Zr-modified Al-Mg alloys processed by selective laser melting, Mater. Des. 115 (2017) 52–63. https://doi.org/10.1016/j.matdes.2016.11.040

[16] A.B. Spierings, K. Dawson, K. Kern, F. Palm, K. Wegener, SLM-processed Sc- and Zr-modified Al-Mg alloy: mechanical properties and microstructural effects of heat

treatment, Mater. Sci. Eng. A 701 (2017) 264–273. https://doi.org/10.1016/j.msea.2017.06.089

[17] K.E. Knipling, D.C Dunand, D.N. Seidman, Criteria for developing castable, creep-resistant aluminum-based alloys – A review, Z. Metallkd. 97 (2006) 246–265. 10.3139/146.101249

[18] J.L. Murray, The Al-Sc (Aluminum-Scandium) System, J. Phase Equil. 19 (1998) 380–384. 10.1361/105497198770342120

[19] J. Røyest, N. Ryum, Scandium in aluminium alloys, Int. Mater. Rev. 50 (2005) 19–44. 10.1179/174328005X14311

[20] C.B. Fuller, D.N. Seidman, D.C. Dunand, Mechanical properties of Al(Sc,Zr) alloys at ambient and elevated temperatures, Acta Mater. 51 (2003) 4803–4814. https://doi.org/10.1016/S1359-6454(03)00320-3

[21] J. Bi, Z. Lei, Y. Chen, X. Chen, N. Lu, Z. Tian, X. Qin, An additively manufactured Al-14.1Mg-0.47Si-0.31Sc-0.17Zr alloy with high specific strength, good thermal stability and excellent corrosion resistance, J. Mater. Sci. Technol. 67 (2021) 23–35. https://doi.org/10.1016/j.jmst.2020.06.036

[22] J. Bi, Z. Lei, Y. Chen, X. Chen. Z. Tian, N. Lu, X. Qin, J. Liang, Microstructure, tensile properties and thermal stability of AlMgSiScZr alloy printed by laser powder bed fusion, J. Mater. Sci. Technol. 69 (2021) 200–211. https://doi.org/10.1016/j.jmst.2020.08.033

[23] R. Li, M. Wang, T. Yuan, B. Song, C. Chen, K. Zhou, P. Cao, Selective laser melting of a novel Sc and Zr modified Al-6.2 Mg alloy: Processing, microstructure, and properties, Powder Technol. 319 (2017) 117–128. https://doi.org/10.1016/j.powtec.2017.06.050

[24] H. Tang, Y. Geng, J. Luo, H. Ju, L. Yu, Mechanical Properties of High Mg-Content Al-Mg-Sc-Zr Alloy Fabricated by Selective Laser Melting, Met. Mater. Int. 27 (2021) 2592–2599. https://doi.org/10.1007/s12540-020-00907-2

[25] D. Bayoumy, D. Schliephake, S. Dietrich, X. Wu, Y.M. Zhu, A.J. Huang, Intensive Processing Optimization for Achieving Ultra-strong and Ductile Al-Mn-Mg-Sc-Zr Alloy Produced by Selective Laser Melting, Mater. Des. 198 (2021) 109317. https://doi.org/10.1016/j.matdes.2020.109317

[26] Q. Jia, F. Zhang, P. Rometsch, J. Li, J. Mata, M. Weyland, L. Bourgeois, M. Sui, X. Wu, Precipitation kinetics, microstructure evolution and mechanical behavior of a developed Al-Mn-Sc alloy fabricated by selective laser melting, Acta Mater. 193 (2020) 239–251. https://doi.org/10.1016/j.actamat.2020.04.015

[27] S. Griffiths, M.D. Rossell, J. Croteau, N.Q. Vo, D.C. Durand, C. Leinenbach, Effect of laser rescanning on the grain microstructure of a selective laser melted Al-Mg-Zr alloy, Mater. Charact. 143 (2018) 34–42. https://doi.org/10.1016/j.matchar.2018.03.033

[28] C.B. Fuller, D.N. Seidman, D.C. Dunand, Creep properties of coarse-grained Al(Sc) alloys at 300°C, Scr. Mater. 40 (1999) 691–696. https://doi.org/10.1016/S1359-6462(98)00468-0

[29] D.N. Seidman, E.A. Marquis, D.C. Dunand, Precipitation strengthening at ambient and elevated temperatures of heat-treatable Al(Sc) alloys, Acta Mater. 50 (2002) 4021–4035. https://doi.org/10.1016/S1359-6454(02)00201-X

[30] H. Rao, S. Giet, K. Yang, X. Wu, C.H.J. Davies, The influence of processing parameters on aluminium alloy A357 manufactured by Selective Laser Melting, Mater. Des. 109 (2016) 334–346. https://doi.org/10.1016/j.matdes.2016.07.009

[31] T.G. Langdon, Grain boundary sliding as a deformation mechanism during creep, Philos. Mag. 178 (1970) 689–700. https://doi.org/10.1080/14786437008220939

[32] H.J. Frost, M.F. Ashby, Deformation mechanism maps, Oxford: Pergamon Press, (1982).

[33] Y. Du, Y. Chang, B. Huang, W. Gong, Z. Jin, H. Xu, Z. Yuan, Y. Liu, Y. He, F.Y. Xie, Diffusion coefficients of some solutes in fcc and liquid Al: critical evaluation and correlation, Mater. Sci. Eng. A 363 (2003) 140–151. https://doi.org/10.1016/S0921-5093(03)00624-5

[34] R.N. Lumley, Fundamentals of Aluminium Metallurgy, Woodhead Publishing, 2011.

[35] A.H. Cottrell, Dislocations and Plastic Flow in Crystals, Report of a Conf. on the Strength of Solids, The Physical Society, London (1948) 30.

[36] K. Ma, H. Wen, T. Hu, T.D. Topping, D. Isheim, D.N. Seidman, E.J. Lavernia, J.M. Schoenung, Mechanical behavior and strengthening mechanismus in ultrafine grain precipitation-strengthened alluminium alloys, Acta Mater. 62 (2014) 141–155. https://doi.org/10.1016/j.actamat.2013.09.042